Supporting information for:

Fully Coherent Triple Sum Frequency Spectroscopy of a Benzene Fermi Resonance

Erin S. Boyle, Andrei V. Pakoulev, and John C. Wright*

Department of Chemistry, University of Wisconsin - Madison, Madison, WI

E-mail: wright@chem.wisc.edu

*To whom correspondence should be addressed

Modeling

Eq. 1 numerically integrates the evolution of the density matrix elements from the initial ρ_{gg} population to the ρ_{eg} output coherence. The program implements this integration in the form

$$\Delta\rho(t) = (\frac{i}{2}\Omega(t)\cdot\rho(t) - \Gamma\rho(t))\Delta t. \tag{1}$$

$\Delta\rho$ (Eq. 1) is found at successive points in time with time increment Δt. The ρ vector contains the Liouville densities in each relevant state of the WMEL diagram and the Γ vector contains corresponding dephasing parameters. All density begins in ρ_{gg} but propagates through the states by the action of Ω. The Ω matrix contains nonzero Ω_{ij} elements only where the chosen pathway allows density to move from ρ_i to ρ_j. In this case the matrix element within the rotating wave approximation is $\pm\mu_{ij}E_k^{\circ}(t)e^{\pm i\omega_k t}e^{\mp i\omega_{ij}t}$, with positive terms representing ket-side transitions and negatives term bra-side, and the phase of the exponential determined by the phase of the interaction. The complex field $E_k(t)$ is calculated at each time increment and is defined by a Gaussian envelope with frequency ω_k. The model requires two time orderings—one for each infrared beam supplying the first interaction—and the resulting ρ_{eg} values were added at each point in time. The output frequency distribution was obtained by Fourier transformation of the ρ_{eg} time dependence, and in cases where the monochromator was simulated, the distribution was apodized with the monochromator filter function. Ω_1, Ω_2, ρ, and Γ for benzene TSF are the following:

$$\Omega_1 = \begin{bmatrix} 0 & 0 & 0 & 0 & 0 \\ \mu_{ag}e^{i\omega_{ag}t}E_1 & 0 & 0 & 0 & 0 \\ 0 & \mu_{2aa}e^{i\omega_{2aa}t}E_2 & 0 & 0 & 0 \\ 0 & \mu_{ba}e^{i\omega_{ba}t}E_2 & 0 & 0 & 0 \\ 0 & 0 & \mu_{e2a}e^{\omega_{e2a}}E_3 & \mu_{eb}e^{\omega_{eb}}E_3 & 0 \\ \end{bmatrix}$$

$$\Omega_2 = \begin{bmatrix} 0 & 0 & 0 & 0 & 0 \\ \mu_{ag}e^{i\omega_{ag}t}E_2 & 0 & 0 & 0 & 0 \\ 0 & \mu_{2aa}e^{i\omega_{2aa}t}E_1 & 0 & 0 & 0 \\ 0 & \mu_{ba}e^{i\omega_{ba}t}E_1 & 0 & 0 & 0 \\ 0 & 0 & \mu_{e2a}e^{\omega_{e2a}}E_3 & \mu_{eb}e^{\omega_{eb}}E_3 & 0 \end{bmatrix}$$

$$\rho = \begin{bmatrix} \rho_{gg} & \rho_{ag} & \rho_{2ag} & \rho_{bg} & \rho_{eg} \end{bmatrix}$$

$$\Gamma = \begin{bmatrix} \Gamma_{gg} = 0 \\ \Gamma_{ag} \\ \Gamma_{2ag} \\ \Gamma_{bg} \\ \Gamma_{eg} = fast \end{bmatrix}$$

Further discussion of TSF 2D frequency scan

Simulations were performed for the Triple Sum Frequency (TSF) spectra in Fig. 3. Fig. S1(a) shows the same experimental data as Fig. 3 but at the amplitude level, and S1(c) performs the same scan with the monochromator tracking $\omega_m = \omega_1 + \omega_2 + \omega_3$. A comparison is done to simulations generated using the approach described in the theoretical section (Figs. S1(b) and S1(d)). As discussed for Fig. 3, these time delays emphasize free induction decay such that $\omega_4 = \omega_{v'g}$. Since $\omega_{v'g}$ is narrower than the 20 cm^{-1} FWHM pulses of ω_1 and ω_2, $\omega_m = \omega_1 + \omega_2 + \omega_3$ will not be equal to ω_4 where ω_1 and ω_2 are either both higher or both lower than the peak central frequency, and the monochromator resolved scan will lose signal at those locations. This gives the peak an antidiagonal character.

One must be cautious in interpretation of these spectra. As discussed in the theory section, driven signal will have the characteristic $\Delta_2 \equiv \omega_{v'g} - \omega_1 - \omega_2 - i\Gamma_{v'g}$, and this will also result in an antidiagonal lineshape. However, this lineshape will be antidiagonal even without monochromator resolution, a characteristic we have observed in spectra collected near zero delay. In the case of

purely driven signal, we predict that tracking the monochromator with $\omega_m = \omega_1 + \omega_2 + \omega_3$ should not result in a change in lineshape.

Finally, it has been noted that the peaks in Figs. 3 and S1 appear especially broad. It is not entirely clear what this is due to, but one contributor is likely poor pulse compression. Models are carried out with pulses having defined temporal duration, matching that which is measured experimentally. This intrinsically defines spectral width, but these spectral widths in reality are often measured to be $\sim$5 cm^{-1} broader than the Fourier transform of their temporal duration would indicate (i.e. 20 cm^{-1} rather than 15 cm^{-1}). Thus the simulation does not perfectly represent the experimental parameters.

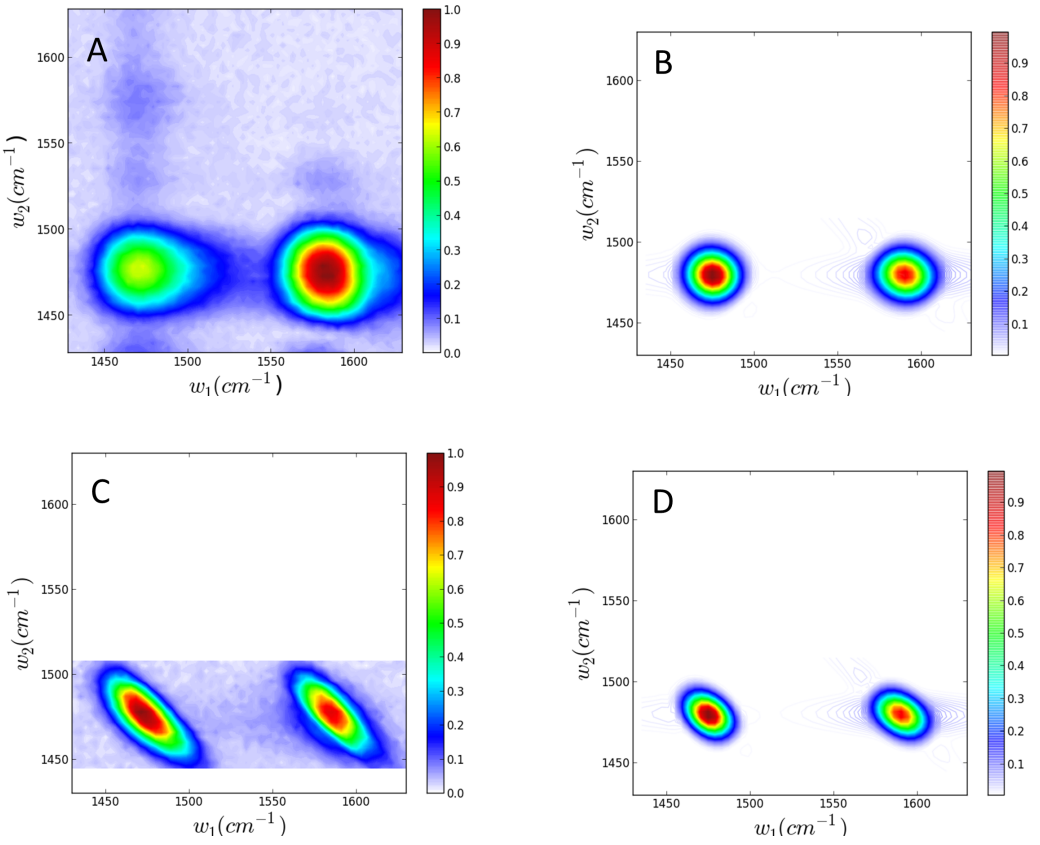

Figure S1: TSF Spectra of 2D frequency scans with τ_{21}=-1.2 ps, τ_{31}=1 ps; all plots at Amplitude level. The left hand spectra ((a) and (c)) are experimental data while the right ((b) and (d)) are simulations of the data using the frequencies and line-widths reported by Bertie.[S1] The top two spectra ((a) and (b)) have the monochromator at zero order (and experimentally use filters to reject ω_3), while the bottom two ((c) and (d)) have spectrally resolved output following $\omega_m = \omega_1 + \omega_2 + \omega_3$ with 11 cm^{-1} resolution.

TSF 2D frequency scan with $2\vec{k}_2+\vec{k}_3$ leak

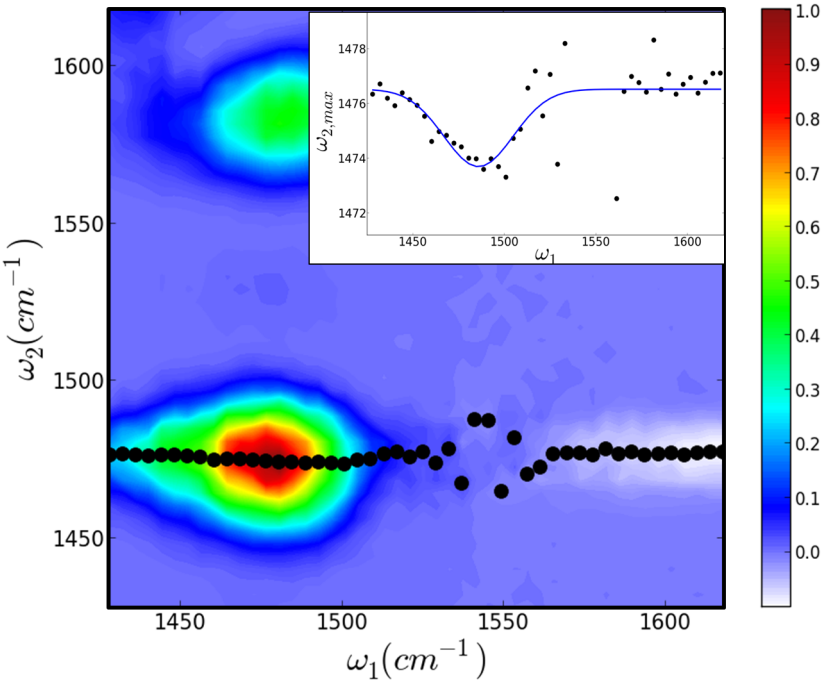

Figure S2: This figure shows the result of subtraction of the average value of the $\vec{k}_4$' signal on the TSF spectrum in Fig. 5 where τ_{21}=1.5 ps and τ_{31}=3 ps. Black data points show the maximum of ω_2 for the $\vec{k}_4$ signal at each ω_1 frequency. The inset plots the maximum ω_2 value as a function of ω_1. The minimum at (ω_1,ω_2)= 1478, 1473.7) cm^{-1} occurs when the $\vec{k}_4$ TSF process is fully resonant with the fundamental and overtone states.

Fig. 5 contains contributions form both the $\vec{k}_4$=$\vec{k}_1+\vec{k}_2+\vec{k}_3$ and $\vec{k}_4$'=$2\vec{k}_2+\vec{k}_3$ TSF signal. The central ω_2 values of the $\vec{k}_4$' horizontal stripe were found by Gaussian fit as discussed in the main body of the paper to extract $\frac{2\omega_{vg}-\delta}{2}$ = 1477.2 cm^{-1}. In order to find the central ω_2 values of $\vec{k}_4$ signal, $\vec{k}_4$' first had to be subtracted. This separation was achieved by subtracting the average intensity of each ω_2 point in the $\vec{k}_4$' region (ω_1=1520-1570 cm^{-1}) from the 2D spectrum to leave only the $\vec{k}_4$ diagonal peak. Diagonal peak ω_2 slices were then fit to a Gaussian profile to accurately define the peak ω_2 frequency as function of ω_1 (Fig. S2 black dots and inset). These central values varied smoothly and showed that the peak center occurs at ω_2=1473.7 cm^{-1}. The difference between the $\vec{k}_4$ and $\vec{k}_4$' peak positions ($\delta/2$) is 3.5 cm^{-1} so δ = 7 cm^{-1}.

Further discussion of TSF Wigner scan

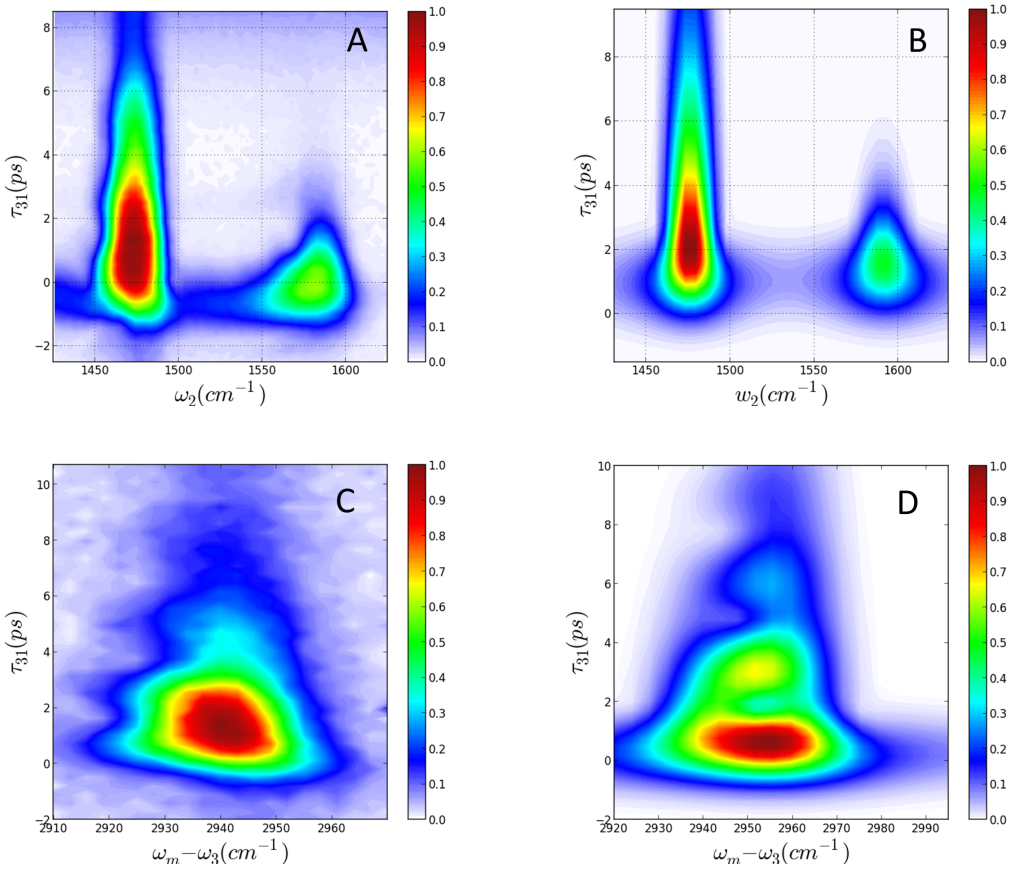

Figure S3: (a) Wigner plot collected with $\tau_{21} = 0$, ω_1=1480 cm^{-1}, and $\omega_m = \omega_1 + \omega_2 + \omega_3$, and (b) model of the same, using dephasing rates predicted in Table 1 and not including additional states. With $\tau_{21} = 0$, ω_1=1480 cm^{-1}, and ω_2=1465 cm^{-1}, beating is present as a function of ω_m and τ_{31} even if ω_2 is not scanned (c). This is simulated in (d) with the inclusion of a secondary state with frequency 2936 cm^1 as appears in the Raman spectrum, and which is excited in proportion to its Raman intensity relative to the 2948 cm^{-1} peak. (All plots at amplitude level.)

The Wigner plot in Fig. S3 traces out the overtone and cross-peak lifetimes of the TSF states. Simulations of this spectrum were obtained using the approach described in the Theory section and assuming dephasing rates predicted by the Raman linewidths of Table 1. The delay times in the simulations were adjusted by 1 ps in order to correct for error in setting the experimental delay times. It was observed that if the monochromator was used to spectrally isolate the output in a Wigner plot, beating occured along for the $2\nu_{13}$ state as a function of the τ_{31} delay time. The peri-

odicity of this beating (∼2.3 ps) indicates a state of about 14 cm^{-1} away generating an interfering output. A mode is visible 12.5 cm^{-1} to the red in the Raman spectrum, and is incorporated into (d) along with a monochromator on the output. It is unclear whether that state is populated directly, or by coherence transfer, and the nature of this state (some combination band) is unconfirmed.

Further discussion of TSF M-factors

Since Triple Sum Frequency (TSF) Coherent Multidimensional Spectroscopy (CMDS) cannot be phase matched for normal refractive index dispersion, it is expected that multidimensional spectra would be strongly influenced by the sample path length, absorption of the excitation beams, and the refractive index dispersion. In order to understand the effects, a series of simulations were performed using the M-factor defined in Eq. 6 and the TSF-CMDS intensity defined in Eq. 7. Eq. 7 assumes the resonances for the first two interactions occur at the peaks of the absorption spectrum but the resonance associated with the second interaction is shifted by 8 cm^{-1} by the Fermi resonance and anharmonic coupling. Thus, the absorption coefficient in the numerator that corresponds to the CMDS enhancements is offset from the absorption coefficients associated with the M-factor. In addition, the line shape of the second resonance is better represented by the line shape of the 2948.5 cm^{-1} Raman in Table 1 and Fig. 2(b). These effects were incorporated into the simulations.

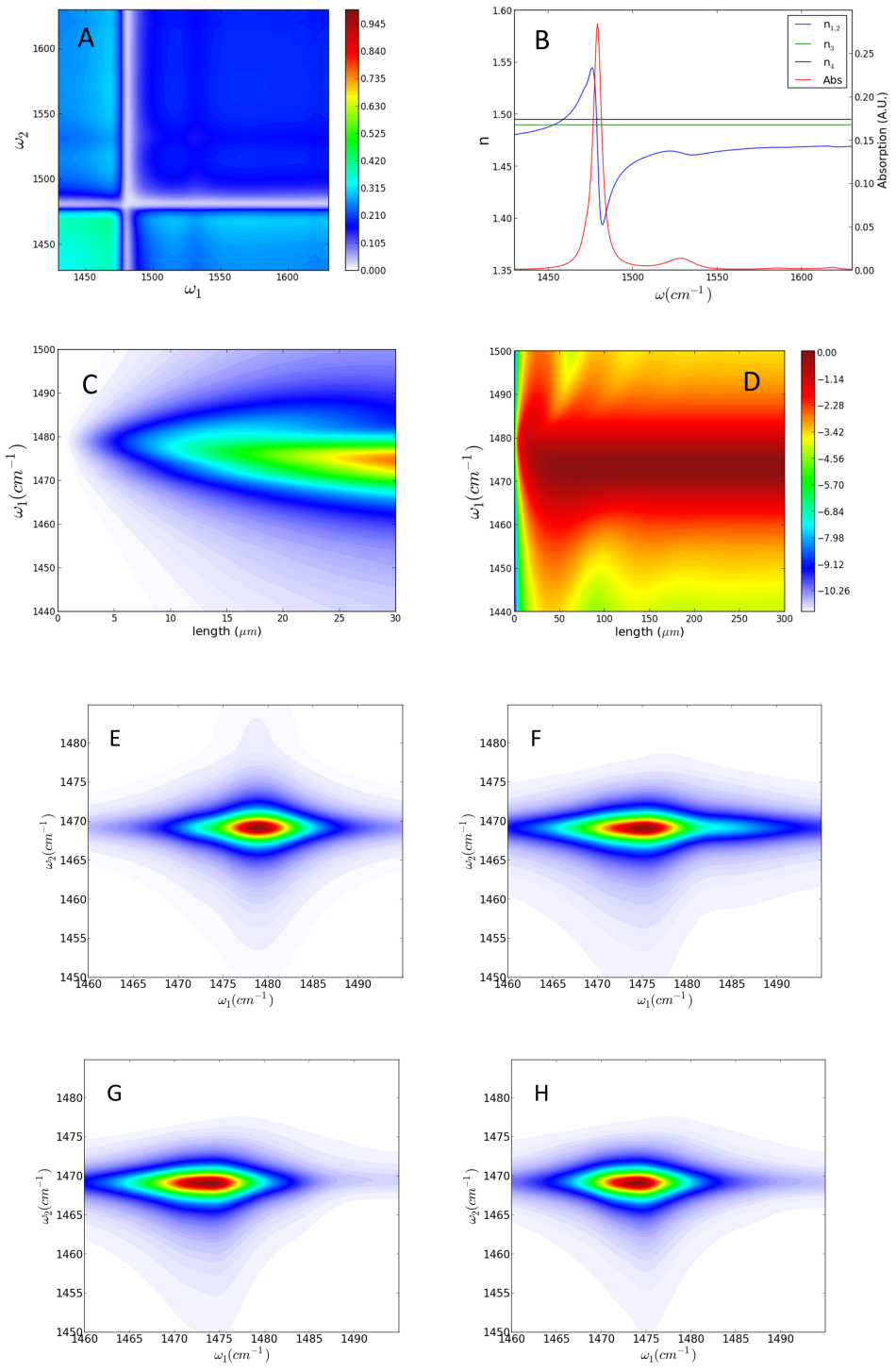

Figure S4: (a) M-factor calculated according to Eq. 6 for a benzene sample with 15 μm path length and $\pm 10^{\circ}$ phase-matching angles using the indices from Bertie[S2,S3] plotted in (b). In (b), the blue trace shows indices as a function of IR frequency, the green and black traces shows the index of refraction at the ω_3 (12,500 cm^{-1}) and ω_4 ($\sim$15,500 cm^{-1}) frequencies, and the red trace gives the absorption through the same region of the infrared. (c) shows the M-factor weighted intensities as a function of path length and (d) shows the same on a logarithmic scale. (e)-(h) show changes in lineshape for 5, 25, 50, and 150 μm path lengths, respectively.

Fig. S4 shows a series of graphs that illustrate the different effects of M-factor. Fig. S4(a) shows the two dimensional dependence of the M-factor on the excitation frequencies using the absorption and refractive index data of Bertie. Fig. S4(b) shows the absorption spectrum and refractive index dispersion over the same region. Fig. S4(c) shows the dependence of the TSF-CMDS intensity on the sample path length and the ω_1 fundamental excitation frequency with ω_2 = 1470 cm^{-1}. The intensity reaches a maximum and then becomes independent of the path length as the increased absorption of the excitation pulses becomes the limiting factor. The peak position also shifts to lower frequency at longer path lengths, as the absorption and refractive index dispersion become more important. The four wave mixing efficiency is improved at ω_1 frequencies that excite the fundamental resonance but are off-set from the strong absorption and asymmetrical phase matching effects (occuring at the center of the fundamental absorption spectrum and to the higher energy side of it, respectively). Fig. S4(d) shows the logarithmic intensity dependence at longer path lengths. The modulations apparent in the spectrum are caused by Brewster fringes arising from the sinc function in Eq. 7. Figs. S4(e)-(h) show a series of two dimensional TSF-CMDS spectral simulations for path lengths ranging from 5 to 150 μm. The peak is off-set from the diagonal by the shift in the resonances for the first and second interactions. There are changes in the asymmetry of the peak and there is the same shift of the peak position along the ω_1 axis. Note that in a true experiment this peak variation of a few cm^{-1} would be convoluted by spectral width of the exciting fields, and would not likely manifest strongly.

References

(S1) Bertie, J. E. John Bertie's Download Site. 2011; `http://www.ualberta.ca/~jbertie/JBDownload.HTM`.

(S2) Bertie, J. E.; Jones, R. N.; Keefe, C. D. Infraeed Intesities of Liquids .12. Accurate Optical Constants and Molar Absorption Coefficients Between 6225 and 500 cm(-1) of Benzene at 25 degrees C, from Spectra Recorded in Several Laboratories. *Appl. Spectrosc.* **1993**, *47*, 891–911.

(S3) Bertie, J. E.; Lan, Z. The Refractive Index of Colorless Liqiods in the Visible and Infrared - Contributions from the Absorption of Infrared and Ultraviolet Radiation and the Electronic Molar Polarizability Below 20500 cm(-1). *J. Chem. Phys.* **1995**, *103*, 10152–10161.